

Simulation of complex viscoelastic flows using Fokker-Planck equation: 3D FENE model

Cédric Chauvière

*Division of Applied Mathematics, Brown University, Box F, Providence, RI
02912, USA*

Alexei Lozinski *

*LMF-ISE-FSTI, Ecole Polytechnique Fédérale de Lausanne, CH-1015 Lausanne,
Switzerland.*

Abstract

This paper is an extension to 3D FENE model of previous work [14] on the simulation of viscoelastic flows using a Fokker-Planck equation, where the 2D FENE model was considered. The Fokker-Planck equation here is discretized using spherical harmonics and Lagrange interpolating polynomial as basis functions. The scheme presented here exhibits the same attractive features as in [14], i.e. noise-free solutions and efficiency. The method is tested for the benchmark problem of a flow past a confined cylinder. Comparisons between the 2D FENE model and the 3D FENE model are made and it is found that the differences between those two models are small for moderate Deborah numbers. It is also found that stochastic simulations of 3D FENE model allow us to reach significantly higher Deborah numbers than that achievable by a similar Fokker-Planck simulations.

1 Introduction

In this work, we are concerned with the incompressible, isothermal and inertialess flow of a FENE viscoelastic fluid in the absence of body forces. For such a fluid, the mass and momentum conservation equations take the form

$$\mathbf{0} = -\nabla p + 2\eta_s \nabla \cdot \varepsilon(\mathbf{v}) + \nabla \cdot \boldsymbol{\tau}, \quad (1)$$

* corresponding author

Email addresses: `cedric@cfm.brown.edu` (Cédric Chauvière),
`alexei.lozinski@epfl.ch` (Alexei Lozinski).

$$\nabla \cdot \mathbf{v} = 0, \quad (2)$$

where \mathbf{v} denotes the fluid velocity, p is the pressure, $\varepsilon(\mathbf{v}) = \frac{1}{2}(\nabla\mathbf{v} + \nabla\mathbf{v}^T)$ is the strain tensor and η_s is the solvent viscosity. The polymeric contribution to the Cauchy stress tensor $\boldsymbol{\tau}$ requires an extra-equation to close the system. This can be done by using the kinetic theory models, in which case the macromolecules are modeled, for example, by dumbbells that consist of two beads connected by a spring (see Fig. 1). At each point in the physical space, the polymeric extra-stress $\boldsymbol{\tau}$ is then computed from the expectation of some functions of \mathbf{q} , where \mathbf{q} is the configuration vector which describes the direction and the elongation of a dumbbell. One of the most popular ways of computing the statistics of the configuration vector is to use the so-called CONFFESSIT approach [17], or its brother the Brownian configuration field method [13], for which a stochastic partial differential equation has to be solved for \mathbf{q} . Note that for those methods, the polymeric extra-stress will suffer from statistical noise, which can be reduced by using variance reduction techniques [3,4].

In the present paper, we follow another route, which consists of computing the probability density function (pdf) $\psi(t, \mathbf{x}, \mathbf{q})$ of \mathbf{q} that is the solution of the Fokker-Planck (FP) equation for the FENE (Finitely Extensible Non-linear Elastic, see Eq. (4) below) dumbbells. For all the numerical experiments carried out in this paper, we suppose that the flow is two dimensional and therefore the centers of mass $\mathbf{x}(t)$ of the dumbbells will stay in a plane. However, there is no physical reason to suppose that the dumbbells lie in the plane of the flow, hence the configuration vector \mathbf{q} should be 3D. For simplicity, one can also consider a reduced model, in which \mathbf{q} is restricted to lie in the plane of the flow. In the latter case, we denote the model as 2D FENE, and in the former case as 3D FENE. The feasibility of using the FP equation for the complex flow of a 2D FENE model was first demonstrated by the authors in [5] and

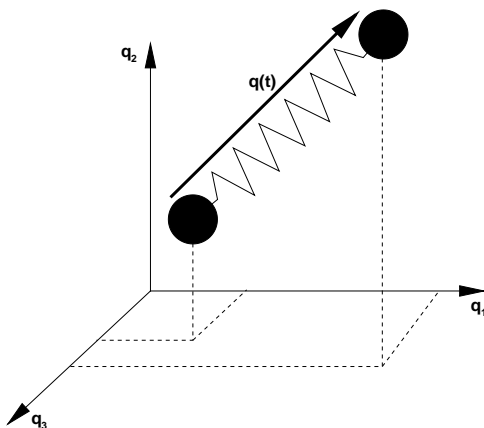


Fig. 1. Description of a single dumbbell placed in the fluid.

the algorithm was significantly improved in a following up paper [14]. In the present paper, we extend the approach used in [14] to 3D FENE model and compare both models for the benchmark problem of the flow around a cylinder in a channel. An exhaustive review of what has been done over the past 15 years or so for the simulations of non-Newtonian flows using the FP equation [1,9–12,15,16] can be found in the introduction of [14] and is not repeated here. We also note that the 3D FENE model was previously investigated in the simple case of the homogeneous shear flow in [9].

The paper is organized as follows: in the next section, we give a detailed expression of the FP equation for the 3D FENE model. Section 3 is devoted to the discretization of the FP equation in configuration space and Section 4 explains how to discretize it efficiently in physical space and time. Having computed the pdf $\psi(t, \mathbf{x}, \mathbf{q})$, we are in position to determine the polymeric extra-stress $\boldsymbol{\tau}$ and this is the topic of Section 5. Section 6 is devoted to the numerical experiments. The direct approach is compared to the stochastic approach in terms of efficiency and accuracy and the comparisons between 2D FENE and 3D FENE models are carried out. Finally, some conclusions are drawn in Section 7.

2 The Fokker-Planck equation for the FENE-3D model

The FP equation for the pdf $\psi(t, \mathbf{x}, \mathbf{q})$ of the random process $\mathbf{q}(t, \mathbf{x})$, that describes the direction and elongation of the 3D FENE dumbbells, reads

$$\frac{D\psi}{Dt} + \operatorname{div}_{\mathbf{q}} \left((\boldsymbol{\kappa}\mathbf{q} - \frac{1}{2\lambda}\mathbf{F}(\mathbf{q}))\psi \right) = \frac{1}{2\lambda}\Delta_{\mathbf{q}}\psi \quad (3)$$

where D/Dt is the material derivative, $\boldsymbol{\kappa}$ is the velocity gradient and the subscript \mathbf{q} in the operators indicates that they act in the configuration space. After some scaling, the spring force of the dumbbells for the FENE model can be written

$$\mathbf{F}(\mathbf{q}) = \frac{\mathbf{q}}{1 - \frac{|\mathbf{q}|^2}{b}}, \quad (4)$$

where b is related to the maximum extensibility of the dumbbell.

For the 3D FENE model, the configuration space is a ball of radius \sqrt{b} and therefore it is natural to represent the vector \mathbf{q} in spherical coordinates

$$q_1 = \rho \sin \theta \cos \varphi, \quad q_2 = \rho \sin \theta \sin \varphi, \quad q_3 = \rho \cos \theta, \quad (5)$$

where $\rho \in [0, \sqrt{b}]$, $\varphi \in [0, 2\pi]$ and $\theta \in [0, \pi]$. We now introduce the unit vector \mathbf{u} defined by

$$\mathbf{q} = \rho \mathbf{u} \quad (6)$$

and the following two operators

$$\Lambda = \frac{\partial}{\partial \mathbf{u}} \cdot (\mathbf{I} - \mathbf{u}\mathbf{u}) \frac{\partial}{\partial \mathbf{u}}, \quad (7)$$

$$\mathcal{L}(\boldsymbol{\kappa})\psi = \frac{\partial}{\partial \mathbf{u}} \cdot [(\mathbf{I} - \mathbf{u}\mathbf{u}) \cdot \boldsymbol{\kappa} \cdot \mathbf{u}\psi]. \quad (8)$$

With those notations, the FP equation (3) takes the form:

$$\frac{D\psi}{Dt} + \mathcal{L}(\boldsymbol{\kappa})\psi + \operatorname{div}_{\mathbf{q}} \left((\rho\boldsymbol{\kappa} : \mathbf{u}\mathbf{u}\mathbf{u} - \frac{1}{2\lambda} \frac{\rho\mathbf{u}}{1 - \rho^2/b})\psi \right) = \frac{1}{2\lambda} \left(\frac{\partial^2}{\partial \rho^2} + \frac{2}{\rho} \frac{\partial}{\partial \rho} + \frac{1}{\rho^2} \Lambda \right) \psi. \quad (9)$$

Expanding the divergence operator, we get

$$\begin{aligned} \frac{D\psi}{Dt} + \mathcal{L}(\boldsymbol{\kappa})\psi + \left(3\boldsymbol{\kappa} : \mathbf{u}\mathbf{u} - \frac{3 - \rho^2/b}{2\lambda(1 - \rho^2/b)^2} \right) \psi + \left(\boldsymbol{\kappa} : \mathbf{u}\mathbf{u} - \frac{1}{2\lambda(1 - \rho^2/b)} \right) \rho \frac{\partial \psi}{\partial \rho} \\ = \frac{1}{2\lambda} \left(\frac{\partial^2}{\partial \rho^2} + \frac{2}{\rho} \frac{\partial}{\partial \rho} + \frac{1}{\rho^2} \Lambda \right) \psi. \end{aligned} \quad (10)$$

The expression above exhibits two singularities for $\rho = 0$ and $\rho = \sqrt{b}$. Those are treated by introducing the transformation of variables

$$\rho^2 = b \frac{1 + \eta}{2} \quad (11)$$

so that $\eta \in (-1, 1)$ if $\rho \in (0, \sqrt{b})$ and

$$\psi = \psi_0 \alpha \text{ with } \psi_0 = \left(\frac{1 - \eta}{2} \right)^s, \quad (12)$$

s being a strictly positive real number. With this change of variable, we note that when $\rho = \sqrt{b}$ ($\eta = 1$), $\psi_0 = 0$ and therefore $\psi = 0$ which is the expected value for the pdf. Similarly, we have $\partial\psi/\partial r = 0$ for $\rho = 0$ (or $\eta = -1$). From now on, we will work with the function $\alpha(t, \mathbf{x}, \eta, \theta, \varphi)$ instead of $\psi(t, \mathbf{x}, \rho, \theta, \varphi)$, so we need to express the operators appearing in (10) in terms of α :

$$\rho \frac{\partial \psi}{\partial \rho} = \psi_0 \left(-\frac{2s(1 + \eta)}{1 - \eta} \alpha + 2(1 + \eta) \frac{\partial \alpha}{\partial \eta} \right), \quad (13)$$

and

$$\begin{aligned} \frac{\partial^2 \psi}{\partial \rho^2} = \psi_0 \left[\left(-\frac{8s}{b(1 - \eta)} + \frac{8s(s - 1)(1 + \eta)}{b(1 - \eta)^2} \right) \alpha + \right. \\ \left. 4 \left(-\frac{4s(1 + \eta)}{b(1 - \eta)} + \frac{1}{b} \right) \frac{\partial \alpha}{\partial \eta} + \frac{8(1 + \eta)}{b} \frac{\partial^2 \alpha}{\partial \eta^2} \right]. \end{aligned} \quad (14)$$

The FP equation (10) can now be rewritten as

$$\frac{D\alpha}{Dt} = -\mathcal{L}(\boldsymbol{\kappa})\alpha - \boldsymbol{\kappa} : \mathbf{u}\mathbf{u} \left(3 - 2s \frac{1+\eta}{1-\eta} \right) \alpha - 2\boldsymbol{\kappa} : \mathbf{u}\mathbf{u} (1+\eta) \frac{\partial\alpha}{\partial\eta} + L_0\alpha \quad (15)$$

where

$$\begin{aligned} L_0\alpha &= \frac{1}{\lambda b(1+\eta)} \Lambda\alpha + \frac{(5-\eta-2s(1+\eta))(b-2s)}{b\lambda(1-\eta)^2} \alpha \\ &+ \frac{2}{b\lambda} \left(3 + (b-4s) \frac{1+\eta}{1-\eta} \right) \frac{\partial\alpha}{\partial\eta} + \frac{4(1+\eta)}{b\lambda} \frac{\partial^2\alpha}{\partial\eta^2} \end{aligned} \quad (16)$$

is the part of the FP operator that does not depend on the velocity gradient.

From now on, we restrict ourselves to the case of a planar divergence-free velocity field, for which the velocity gradient takes the form

$$\boldsymbol{\kappa} = \begin{pmatrix} \kappa_{11} & \kappa_{12} & 0 \\ \kappa_{21} & -\kappa_{11} & 0 \\ 0 & 0 & 0 \end{pmatrix}. \quad (17)$$

We want to transform Eq. (15) in a way analogous to that described in [14], which will enable us to apply the fast solver proposed there. To achieve this, we decompose the velocity gradient into symmetric and antisymmetric parts and rotate the coordinates to the principal axes of the symmetric part. We have thus

$$\boldsymbol{\kappa} = k\boldsymbol{\pi}_\phi \mathbf{I}_s \boldsymbol{\pi}_{-\phi} + k_a \mathbf{I}_a \quad (18)$$

where \mathbf{I}_s and \mathbf{I}_a are the constant matrices

$$\mathbf{I}_s = \begin{pmatrix} 1 & 0 & 0 \\ 0 & -1 & 0 \\ 0 & 0 & 0 \end{pmatrix}, \quad \mathbf{I}_a = \begin{pmatrix} 0 & 1 & 0 \\ -1 & 0 & 0 \\ 0 & 0 & 0 \end{pmatrix}, \quad (19)$$

and $\boldsymbol{\pi}_\phi$ is the matrix of the rotation by angle ϕ in 12-plane

$$\boldsymbol{\pi}_\phi = \begin{pmatrix} \cos\phi & -\sin\phi & 0 \\ \sin\phi & \cos\phi & 0 \\ 0 & 0 & 1 \end{pmatrix}.$$

The scalars k , ϕ and k_a appearing in (18) are calculated from $\boldsymbol{\kappa}$ via

$$k = \sqrt{\kappa_{11}^2 + (\kappa_{12} + \kappa_{21})^2/4}, \quad (20)$$

$$\phi = \frac{1}{2} \arctan \left(\frac{\kappa_{12} + \kappa_{21}}{2\kappa_{11}} \right), \quad (21)$$

and

$$k_a = \frac{\kappa_{12} - \kappa_{21}}{2}. \quad (22)$$

Let Π_ϕ be the operator defined for an arbitrary function on the unit sphere $\Phi(\varphi, \theta)$ by

$$\Pi_\phi \Phi(\varphi, \theta) = \Phi(\varphi + \phi, \theta), \quad (23)$$

i.e. the result of the rotation of coordinates $\boldsymbol{\pi}_{-\phi}$. Substituting (18) into (15) and using the notation (23) and the fact that $\mathcal{L}(\mathbf{I}_a) = -\partial/\partial\varphi$ (see Appendix A.1) and $\mathbf{I}_a : \mathbf{u}\mathbf{u} = 0$, we arrive at the desired form of the FP equation

$$\frac{D\alpha}{Dt} = k\Pi_{-\phi}L_1\Pi_\phi\alpha + k_a\frac{\partial\alpha}{\partial\varphi} + L_0\alpha \quad (24)$$

where

$$L_1 = -\mathcal{L}(\mathbf{I}_s) - \mathbf{I}_s : \mathbf{u}\mathbf{u} \left(3 - 2s\frac{1+\eta}{1-\eta} \right) - 2\mathbf{I}_s : \mathbf{u}\mathbf{u}(1+\eta)\frac{\partial}{\partial\eta}. \quad (25)$$

3 Discretization in configuration space

A discrete approximation of the unknown function $\alpha(t, \mathbf{x}, \eta, \theta, \varphi)$ may be written as

$$\alpha_N(t, \mathbf{x}, \eta, \theta, \varphi) = \sum_{i=0}^1 \sum_{l=0}^{N_\eta} \sum_{n=0}^{N_u} \sum_{m=i}^n \alpha_{i,l,n,m}(t, \mathbf{x}) \Phi_{2n,2m}^i(\theta, \varphi) h_l(\eta), \quad (26)$$

where $\Phi_{n,m}^i(\theta, \varphi) = P_n^m(\cos\theta) \cos\left(m\varphi - i\frac{\pi}{2}\right)$ are spherical harmonics and P_n^m are the associated Legendre polynomials. $h_l(\eta)$ are Lagrange interpolating polynomials of order N_η based on the Gauss-Jacobi points η_k , that is $h_l(\eta_k) = \delta_{lk}$. In (26), only the spherical harmonics of even order appear because α is an even function of \mathbf{u} .

To discretize the operators L_0 and L_1 we insert (26) into (16) and (25), form the products with test functions $\Phi_{2n,2m}^i(\theta, \varphi) h_l(\eta)$ multiplied by a weight function and integrate over the configuration space. In doing so, the integrals with respect to θ and φ can be evaluated exactly since the spherical harmonics form the orthogonal basis in L_2 space on the unit sphere. For the integrals with respect to η , we resort to Gaussian quadrature rule over the interval $[-1, 1]$, i.e.

$$(u, v)_{J_\alpha, J_\beta} \simeq \sum_{k=0}^{N_\eta} \omega_k u(\eta_k) v(\eta_k), \quad (27)$$

where ω_k are the quadrature weights associated with the Gauss-Jacobi points $\{\eta_k\}_{k=0,\dots,N_\eta}$ and the scalar product $(\cdot, \cdot)_{J_\alpha, J_\beta}$ is defined by

$$(u, v)_{J_\alpha, J_\beta} = \int_{-1}^1 (1 - \eta)^{J_\alpha} (1 + \eta)^{J_\beta} u(\eta) v(\eta) d\eta, \quad (28)$$

where J_α and J_β are real numbers.

We note also that the spherical harmonics are the eigenfunctions of the Laplace operator on the unit sphere, so we have

$$\Lambda \Phi_{n,m}^i = -n(n+1) \Phi_{n,m}^i.$$

In the way, outlined in the preceding paragraph, we can now write the discretization \mathbf{L}_0 of the operator L_0 :

$$\mathbf{L}_0 \alpha_N(t, \mathbf{x}, \eta, \theta, \varphi) = \sum_{i=0}^1 \sum_{l=0}^{N_\eta} \sum_{n=0}^{N_u} \sum_{m=i}^n (L_0 \alpha)_{i,l,n,m}(t, \mathbf{x}) \Phi_{2n,2m}^i(\theta, \varphi) h_l(\eta) \quad (29)$$

where

$$\begin{aligned} (L_0 \alpha)_{i,l,n,m} = & \left(-\frac{2n(2n+1)}{\lambda b(1+\eta_l)} + \frac{(5-\eta_l-2s(1+\eta_l))(b-2s)}{b\lambda(1-\eta_l)^2} \right) \alpha_{i,l,n,m} \\ & + \frac{2}{b\lambda} \left(3 + (b-4s) \frac{1+\eta_l}{1-\eta_l} \right) \sum_{p=0}^{N_\eta} h'_p(\eta_l) \alpha_{i,p,n,m} \\ & + \frac{4(1+\eta_l)}{b\lambda} \sum_{p=0}^{N_\eta} h''_p(\eta_l) \alpha_{i,p,n,m}. \end{aligned} \quad (30)$$

In the case of the operator L_1 we need also the discretizations of operators $\mathcal{L}(\mathbf{I}_s)$ and $\mathbf{I}_s : \mathbf{u}\mathbf{u}$. Such an expression on a the spherical harmonics basis can be obtained by noticing that

$$\mathcal{L}(\mathbf{I}_s) \Phi_{n,m}^i = \sum_{k=m-2}^{m+2} \sum_{j=n-2}^{n+2} a_{nj}^{mk} \Phi_{j,k}^i \quad (31)$$

and

$$\mathbf{I}_s : \mathbf{u}\mathbf{u} \Phi_{n,m}^i = \sum_{k=m-2}^{m+2} \sum_{j=n-2}^{n+2} b_{nj}^{mk} \Phi_{j,k}^i. \quad (32)$$

All the non-zero coefficients a_{nj}^{mk} and b_{nj}^{mk} are given in Tables 1 and 2, respectively. The derivation of these formulas is non-trivial and the details are given in Appendix A. Note that (31) is the special case of the discretization of $\mathcal{L}(\boldsymbol{\kappa})$, which is explicitly given in [11] for rather general form of $\boldsymbol{\kappa}$.

Table 1

Table of coefficients appearing in the discretization of the operator $\mathcal{L}(\mathbf{I}_s)$

$a_{n,n-2}^{m,m-2}$	$\frac{(n-2)(n+m)(n+m-1)(n+m-2)(n+m-3)(1-\delta_{m0})}{2(2n+1)(2n-1)}$
$a_{n,n}^{m,m-2}$	$\frac{3(n+m)(n+m-1)(n-m+1)(n-m+2)(1-\delta_{m0})}{2(2n+1)(2n+3)}$
$a_{n,n+2}^{m,m-2}$	$-\frac{(n+3)(n-m+1)(n-m+2)(n-m+3)(n-m+4)(1-\delta_{m0})}{2(2n+1)(2n+3)}$
$a_{n,n-2}^{m,m+2}$	$\frac{(n-2)(1+\delta_{m0})}{2(2n+1)(2n-1)}$
$a_{n,n}^{m,m+2}$	$\frac{3(1+\delta_{m0})}{2(2n+1)(2n+3)}$
$a_{n,n+2}^{m,m+2}$	$-\frac{(n+3)(1+\delta_{m0})}{2(2n+1)(2n+3)}$

Table 2

Table of coefficients appearing in the discretization of the operator $\mathbf{I}_s : \mathbf{u}\mathbf{u}$

$b_{n,n-2}^{m,m-2}$	$\frac{(n+m)(n+m-1)(n+m-2)(n+m-3)(1-\delta_{m0})}{2(2n+1)(2n-1)}$
$b_{n,n}^{m,m-2}$	$\frac{(n-m+2)(n+m-1)(m(m-1)-n(n+1))}{(2n+1)(2n+3)}$
$b_{n,n+2}^{m,m-2}$	$\frac{(n-m+1)(n-m+2)(n-m+3)(n-m+4)(1-\delta_{m0})}{2(2n+1)(2n+3)}$
$b_{n,n-2}^{m,m+2}$	$\frac{1+\delta_{m0}}{2(2n+1)(2n-1)}$
$b_{n,n}^{m,m+2}$	$-\frac{1+\delta_{m0}}{(2n+1)(2n+3)}$
$b_{n,n+2}^{m,m+2}$	$\frac{1+\delta_{m0}}{2(2n+1)(2n+3)}$

We can now write the discretization \mathbf{L}_1 of the operator L_1 using the notation analogous to that used for the operator L_0 in (29)-(30):

$$\begin{aligned}
(L_1\alpha)_{i,l,n,m} = & - \sum_{k=m-1}^{m+1} \sum_{j=n-1}^{n+1} \left[a_{2j,2n}^{2k,2m} \alpha_{i,l,j,k} + \left(3 - 2s \frac{1+\eta_l}{1-\eta_l} \right) b_{2j,2n}^{2k,2m} \alpha_{i,l,j,k} \right. \\
& \left. + 2(1+\eta_l) \sum_{p=0}^{N_\eta} h'_p(\eta_l) b_{2j,2n}^{2k,2m} \alpha_{i,p,j,k} \right]. \quad (33)
\end{aligned}$$

To conclude this section, we note that the rotation operator Π_ϕ is discretized easily since trigonometric functions are used in (26) to represent the dependence of α on φ .

4 Discretization in physical space and time

Due to the stiffness of the discrete operators resulting from (15), an explicit time discretization would require very small time steps in order to be stable. For efficiency reasons, an implicit time integration scheme is therefore required. Fortunately, such an implicit scheme is made tractable due to a separation of the operators acting in the physical space from the one acting in the configuration space and leading to a time splitting. Furthermore, the configuration step can be optimized by using the form of FP equation with rotations in φ (see Eq. (24)). The motivation and implementation of these ideas are explained in detail in [14] for the 2D FENE model and will not be repeated here. We only provide the resulting time-splitting scheme:

Suppose we have the solution α^n at time $t_n = n\Delta t$. We perform the following two steps:

- Configuration step for the intermediate unknown $\alpha^{n+1/2}$:

$$\alpha^{n+1/2} = \Pi_{\frac{1}{2}k_a\Delta t-\phi} \mathbf{P} (\mathbf{I} - k\mathbf{D})^{-1} \mathbf{P}^{-1} (\mathbf{R} + k\mathbf{M}) \Pi_{\phi+\frac{1}{2}k_a\Delta t} \alpha^n \quad (34)$$

where

$$\mathbf{M} = \frac{\Delta t}{2} \left(\mathbf{I} - \frac{\Delta t}{2} \mathbf{L}_0 \right)^{-1} \mathbf{L}_1,$$

and

$$\mathbf{R} = \left(\mathbf{I} - \frac{\Delta t}{2} \mathbf{L}_0 \right)^{-1} \left(\mathbf{I} + \frac{\Delta t}{2} \mathbf{L}_0 \right).$$

In (34), \mathbf{P} is the matrix formed by the eigenvectors of \mathbf{M} and \mathbf{D} is the diagonal matrix formed with the eigenvalues of \mathbf{M} so that $\mathbf{M} = \mathbf{P}\mathbf{D}\mathbf{P}^{-1}$. The operation (34) should be performed at each grid point in the physical space with the parameters k , ϕ and k_a based on the velocity gradient at that point and calculated via the formulas (20)–(22). We note that all the matrices appearing in (34) are constant and hence can be computed once for all. Inverting the matrix $(\mathbf{I} - k\mathbf{D})$ is very cheap since \mathbf{D} is diagonal. Therefore, our configuration step involves essentially only matrix-vector multiplications and is relatively inexpensive.

- Physical step for the computation of α^{n+1} :

$$\frac{\alpha^{n+1} - \alpha^{n+1/2}}{\Delta t} + \mathbf{v} \cdot \nabla \alpha^{n+1} = 0. \quad (35)$$

This equation should be solved by a numerical method appropriate for hyperbolic PDEs, and here we use the spectral element method described in [6].

5 Computation of the polymeric extra-stress

Having computed the pdf $\psi(t, \mathbf{x}, \mathbf{q})$ in \mathbf{x} at time t , the extra-stress which will serve as a source term for the Stokes equations can be computed using Kramer's expression (see page 69 of [2])

$$\begin{aligned}\boldsymbol{\tau}(\mathbf{x}, t) &= \frac{\eta_p}{\lambda} \left(\frac{b+5}{b} \right) (-\mathbf{I} + \langle \mathbf{q} \otimes \mathbf{F}(\mathbf{q}) \rangle) \\ &= \frac{\eta_p}{\lambda} \left(\frac{b+5}{b} \right) \left(-\mathbf{I} + \int_{|\mathbf{q}|^2 < b} \mathbf{q} \otimes \mathbf{F}(\mathbf{q}) \psi(t, \mathbf{x}, \mathbf{q}) d\mathbf{q} \right).\end{aligned}\quad (36)$$

Using (4), (6) and (11), an expression for $\mathbf{q} \otimes \mathbf{F}(\mathbf{q})$ is

$$\mathbf{q} \otimes \mathbf{F}(\mathbf{q}) = \frac{\rho^2}{1 - \frac{\rho^2}{b}} \mathbf{u} \otimes \mathbf{u} = b \left(\frac{1+\eta}{1-\eta} \right) \mathbf{u} \otimes \mathbf{u}.\quad (37)$$

The pdf $\psi(t, \mathbf{x}, \mathbf{q})$ appearing in the integrand of (36) can be replaced by a function of $\alpha(t, \mathbf{x}, \mathbf{q})$ to get

$$\begin{aligned}& \int_{|\mathbf{q}|^2 < b} \mathbf{q} \otimes \mathbf{F}(\mathbf{q}) \psi(t, \mathbf{x}, \mathbf{q}) d\mathbf{q} \\ &= \int_{-1}^1 \int_0^{2\pi} \int_0^\pi \frac{b^{5/2}}{2^{5/2+s}} (1+\eta)^{3/2} (1-\eta)^{s-1} \alpha(t, \mathbf{x}, \mathbf{q}) \mathbf{u} \otimes \mathbf{u} d\theta d\varphi d\eta.\end{aligned}\quad (38)$$

We then replace $\alpha(t, \mathbf{x}, \mathbf{q})$ in the above integral by its discrete representation (26), evaluate the integrals with respect to θ and φ analytically and the integral with respect to η numerically. Most of the terms vanish and we get the following expressions for the three components of the extra-stress at each point (t, \mathbf{x}) :

$$\begin{aligned}\tau_{xx} &= \frac{\eta_p}{\lambda} \frac{b+5}{b} \left(-1 + \frac{\pi b^{5/2}}{2^{s+1/2}} \sum_{l=0}^{N_\eta} \omega_l (1+\eta_l)^{3/2-J_\beta} (1-\eta_l)^{s-1-J_\alpha} \right. \\ &\quad \left. \left(\frac{1}{3} \alpha_{0,l,0,0} - \frac{1}{15} \alpha_{0,l,1,0} + \frac{2}{5} \alpha_{0,l,1,1} \right) \right), \\ \tau_{xy} &= \frac{\eta_p}{\lambda} \frac{b+5}{b} \frac{\pi b^{5/2}}{2^{s+1/2}} \frac{2}{5} \sum_{l=0}^{N_\eta} \omega_l (1+\eta_l)^{3/2-J_\beta} (1-\eta_l)^{s-1-J_\alpha} \alpha_{1,l,1,1},\end{aligned}$$

$$\tau_{yy} = \frac{\eta_p b + 5}{\lambda b} \left(-1 + \frac{\pi b^{5/2}}{2^{s+1/2}} \sum_{l=0}^{N_\eta} \omega_l (1 + \eta_l)^{3/2 - J_\beta} (1 - \eta_l)^{s-1 - J_\alpha} \left(\frac{1}{3} \alpha_{0,l,0,0} - \frac{1}{15} \alpha_{0,l,1,0} - \frac{2}{5} \alpha_{0,l,1,1} \right) \right),$$

$$\tau_{zz} = \frac{\eta_p b + 5}{\lambda b} \left(-1 + \frac{\pi b^{5/2}}{2^{s+1/2}} \sum_{l=0}^{N_\eta} \omega_l (1 + \eta_l)^{3/2 - J_\beta} (1 - \eta_l)^{s-1 - J_\alpha} \left(\frac{1}{3} \alpha_{0,l,0,0} + \frac{2}{15} \alpha_{0,l,1,0} \right) \right)$$

where ω_l are the the quadrature weights from (27).

6 Numerical experiments

6.1 The benchmark problem

The performance of our solver is tested by solving the benchmark problem of planar viscoelastic flow around a cylinder confined in a channel (see Fig. 2). This problem was chosen for its ability to present different types of flows over the domain: shear flow near solid walls and extensional flow in the wake of the cylinder. Furthermore, the flow domain does not have geometrical singularities, which makes it suitable for high order type of discretization. As is usually done in the literature for this problem (see [7,8,19,20] for example), we take the ratio of the half width of the channel H to the radius of the cylinder R to be equal to two. For similar reasons, the ratio of solvent to total viscosities is taken to be $\eta_s/(\eta_s + \eta_p) = 0.59$. For this problem, a global Deborah number may be

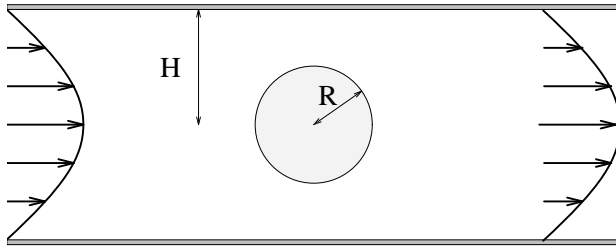


Fig. 2. Cylinder radius R placed symmetrically in a 2D channel of half width H .

defined by

$$De = \frac{\lambda \bar{U}}{R}, \quad (39)$$

where \bar{U} is the average velocity of the fluid in the channel at entry or exit. For all our numerical experiments, the parameter b in (36) is taken equal to 10. The Stokes problem (1)-(2) is decoupled from the computation of the polymeric extra-stress in a standard way and it is solved using the spectral element method (see [18] for details). The physical domain is divided into 26 elements and polynomials of degree $N = 6$ are used in each element and each spatial direction. To save in computational time, we assume that the solution is symmetric with respect to the axis $y = 0$ and therefore, only half of the domain needs to be meshed. The length of the channel is 40 times the cylinder radius, so that we can use periodic boundaries conditions for the velocity and extra-stress at inflow and outflow by assuming that the periodic cylinders do not influence each other. For the FP simulation, the iterations are stopped when the following convergence criterion is fulfilled for all collocation points $\mathbf{x} \in \Omega$:

$$\frac{|\mathbf{v}^{i+1}(\mathbf{x}) - \mathbf{v}^i(\mathbf{x})|}{\Delta t} \leq 10^{-4}. \quad (40)$$

The approach presented here is compared with a standard stochastic simulation using the Brownian configuration field method. The stochastic approach is presented in detail in [14] for the 2D FENE model and the extension from 2D to 3D is trivial. For all our simulations (deterministic or stochastic), the time step Δt is chosen equal to 0.01. Note that for the stochastic simulation, a stopping criterion like (40) cannot be used because of the presence of noise in the computed solutions and the simulations are arbitrarily stopped instead at $t = 6$. We take $N_u = 6$ and $N_\eta = 12$ for the discretization in the configuration space (see formula (26)). The value of s in (12) is taken equal to 2.5 and we take $J_\alpha = J_\beta = 0.5$ in (28). There is no theoretical justification for choosing those values, they have been found after some numerical experiments to give a good compromise between accuracy and stability.

6.2 Comparison between the stochastic approach and the deterministic approach

We define the drag factor F^* on the cylinder by:

$$F^* = \frac{F}{4\pi(\eta_s + \eta_p)\bar{U}}, \quad (41)$$

where F is the drag on the cylinder. Figure 3 shows the value of the drag factor as a function of time for the stochastic simulation using 16000 realizations for the 2D and the 3D FENE models at a Deborah number 0.6. For the stochastic

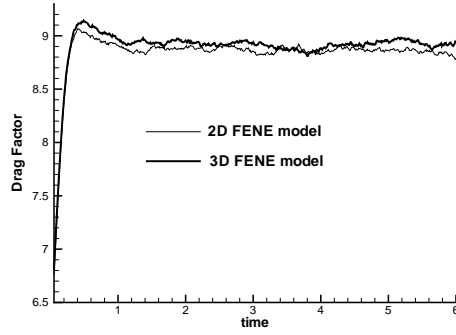


Fig. 3. Drag factor as a function of time for the 2D and 3D FENE models with a stochastic simulation using 16000 realizations at $De = 0.6$.

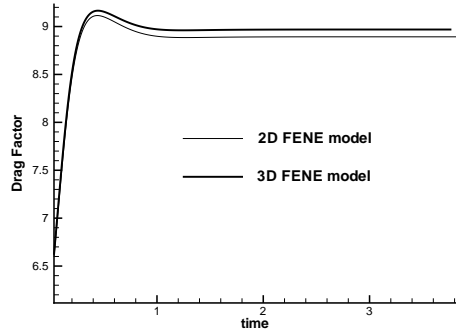


Fig. 4. Drag factor as a function of time for the 2D and 3D FENE models using the Fokker-Planck equation at $De = 0.6$.

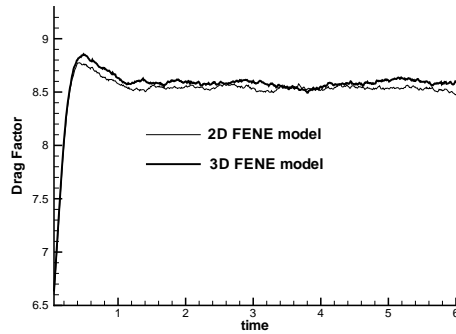


Fig. 5. Drag factor as a function of time for the 2D and 3D FENE models with a stochastic simulation using 16000 realizations at $De = 0.9$.

simulation, the magnitude of the noise in computed solutions is proportional to $1/\sqrt{M}$, where M is the number of realizations. Therefore, in Fig. 3, the magnitude of the noise is such that it is difficult to conclude which model (2D or 3D) gives the highest drag factor. On the other hand, the FP simulation

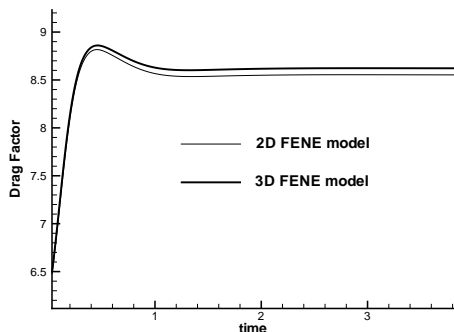


Fig. 6. Drag factor as a function of time for the 2D and 3D FENE models using the Fokker-Planck equation at $De = 0.9$.

Table 3

Comparison of the CPU cost per time step for the direct approach and for the stochastic approach (3D FENE model).

Fokker-Planck	Stochastic-1000	Stochastic-16000
7.1	12.6	202.0

is deterministic and for the same problem and same parameters, the results shown in Fig. 4 clearly indicate that the drag factor of the 3D FENE model is higher than the drag factor of the 2D FENE model. The same kind of results are reproduced in Fig. 5 and 6, but for a higher Deborah number ($De = 0.9$) and the conclusions remain the same. Not only is the FP approach more accurate than its stochastic counterpart, but it is also more efficient in terms of CPU cost. This can be seen from table 3 which gives the average CPU time per time step for a computation performed on a Pentium IV 1.5GHz processor. Solving the FP equation is about 1.8 times faster than solving the stochastic equation with 1000 realizations. Note that, as can be expected, the stochastic approach with 16000 realizations is about 16 times slower than the same computation with only 1000 samples.

6.3 Comparison between 2D FENE and 3D FENE models

Based on the drag factor (see Fig. 4 or Fig. 6), it seems that the difference between the 2D FENE model and the 3D FENE model are small. Such a finding is confirmed on Figs. 7-9 which show respectively the differences in the xx , xy and yy components of the extra-stress between the 2D and 3D FENE models at $De = 0.6$. The small black square indicates the location of maximal absolute difference. As can be seen from the values of the contour level, the differences between the two models is small for all components all over the domain. In all cases, the maximum difference is located on the cylinder

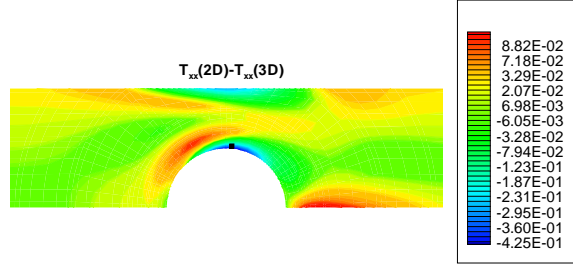


Fig. 7. Difference of the xx component of the extra-stress between the 2D and the 3D FENE model at $De = 0.6$.

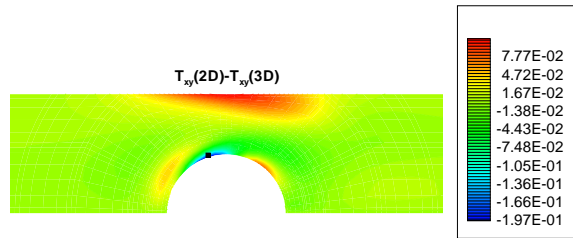


Fig. 8. Difference of the xy component of the extra-stress between the 2D and the 3D FENE model at $De = 0.6$.

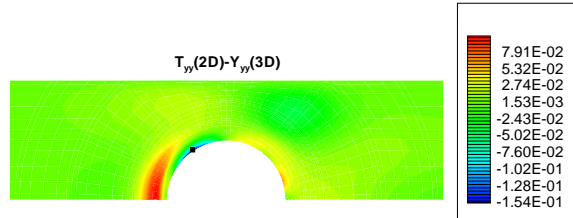


Fig. 9. Difference of the yy component of the extra-stress between the 2D and the 3D FENE model at $De = 0.6$.

surface, where we have strong shear flow. Results at a Deborah number 0.9 are very similar and they are not reproduced here. Such an investigation would not have been possible using a stochastic approach since the difference between the two models would have been of the order of magnitude of the noise. The fact that we can use the 2D FENE model instead of the 3D model without major changes in the solution is important from a computational point of view, since solving the FP in a 2D configuration space is one order of magnitude cheaper than solving it in a 3D configuration space. On the other hand, for the stochastic approach, going from 2D to 3D is not so critical since it only requires one extra equation to be solved for q_z .

6.4 Maximum Deborah number achievable

The maximum Deborah number that could be achieved for the 3D FENE model using the FP equation is $De = 1.1$. However, convergence with mesh refinement (both in the physical space and in the configuration space) was only possible up to $De = 0.9$ and this is why in the previous section we only present results up to this Deborah number. The difficulty, as we increase the Deborah number, comes from the fact that the flow may be strong in some area of the domain, leading to a pdf with extremely localized features, which are very difficult to capture numerically. In contrast, the limiting Deborah numbers of the stochastic approach were found to be around $De = 4.0$. This situation is quite different from what we have observed in our 2D FENE simulations [14]. The maximum Deborah number achievable in the latter case was about 1.2 both for stochastic and deterministic approaches.

7 Conclusions

In this paper, we have presented an efficient numerical method for the discretization of the FP equation for the 3D FENE model. The details of the method were given in the context of high order methods using spherical harmonics and high order polynomials for the discretization in the configuration space. For the flow past a confined cylinder, the resulting solver was shown to be more efficient than doing a stochastic simulation using the Brownian configuration field technique. Furthermore, contrary to stochastic simulations, this direct approach gives solutions that are noise-free. It was also found that for the complex flow around a cylinder, the differences of results between the 2D FENE model and the 3D FENE model are small. In terms of stability, the advantage is still for the stochastic approach and future work will be dedicated to making the FP simulations more stable in order to reach higher Deborah numbers.

Acknowledgment

The second author was supported by the Swiss National Science Foundation, grant number 2100-057119.

A Appendix

The purpose of this appendix is to give the expressions in spherical coordinates of the operators $\mathcal{L}(\boldsymbol{\kappa})$ and $\mathbf{I}_s : \mathbf{u}\mathbf{u}$ and to compute the effect of the operators

$\mathcal{L}(\mathbf{I}_s)$ and $\mathbf{I}_s : \mathbf{u}\mathbf{u}$ on spherical harmonics $\Phi_{n,m}^i$.

A.1 Operators $\mathcal{L}(\mathbf{I}_s)$ and $\mathcal{L}(\mathbf{I}_a)$

The operator $\mathcal{L}(\boldsymbol{\kappa})$ defined by (8) can be written in spherical coordinates as

$$\begin{aligned}\mathcal{L}(\boldsymbol{\kappa})\psi &= \left(\mathbf{e}_\varphi \frac{1}{\sin\theta} \frac{\partial}{\partial\varphi} + \mathbf{e}_\theta \frac{\partial}{\partial\theta} \right) \cdot (A_\varphi\psi\mathbf{e}_\varphi + A_\theta\psi\mathbf{e}_\theta) \\ &= \frac{1}{\sin\theta} \left[\frac{\partial}{\partial\varphi}(A_\varphi\psi) + \frac{\partial}{\partial\theta}(\sin\theta A_\theta\psi) \right]\end{aligned}\quad (\text{A.1})$$

where $A_\varphi = \boldsymbol{\kappa}\mathbf{u} \cdot \mathbf{e}_\varphi$ and $A_\theta = \boldsymbol{\kappa}\mathbf{u} \cdot \mathbf{e}_\theta$.

In the special case $\boldsymbol{\kappa} = \mathbf{I}_a$, we have $A_\varphi = -\sin\theta$ and $A_\theta = 0$, so that $\mathcal{L}(\mathbf{I}_a) = -\partial/\partial\varphi$. Setting $\boldsymbol{\kappa} = \mathbf{I}_s$, we obtain

$$A_\varphi = -\sin 2\varphi \sin\theta \quad \text{and} \quad A_\theta = \cos 2\varphi \sin\theta \cos\theta.$$

Plugging the above expression for A_θ and A_φ into (A.1), we get after simplifications

$$\mathcal{L}(\mathbf{I}_s)\psi = -\sin 2\varphi \frac{\partial\psi}{\partial\varphi} + \cos 2\varphi \left(-3\sin^2\theta\psi + \sin\theta \cos\theta \frac{\partial\psi}{\partial\theta} \right) \quad (\text{A.2})$$

Let's put $\psi = \Phi_{n,m}^i = P_n^m(\cos\theta) \cos\left(m\varphi - i\frac{\pi}{2}\right)$ in (A.2), then we get

$$\begin{aligned}\mathcal{L}(\mathbf{I}_s)\Phi_{n,m}^i &= m \sin 2\varphi \sin\left(m\varphi - i\frac{\pi}{2}\right) \cdot P_n^m(\cos\theta) \\ &\quad + \cos 2\varphi \cos\left(m\varphi - i\frac{\pi}{2}\right) \cdot S_n^m(\cos\theta)\end{aligned}$$

where

$$S_n^m(x) = (x^2 - 1) \left(3P_n^m(x) + x \frac{d}{dx} P_n^m(x) \right).$$

or, with $x = \cos\theta$,

$$\begin{aligned}\mathcal{L}(\mathbf{I}_s)\Phi_{n,m}^i &= \frac{1}{2} \left[\cos\left((m+2)\varphi - i\frac{\pi}{2}\right) (-mP_n^m(x) + S_n^m(x)) \right. \\ &\quad \left. + \cos\left((m-2)\varphi - i\frac{\pi}{2}\right) (mP_n^m(x) + S_n^m(x)) \right]\end{aligned}\quad (\text{A.3})$$

In the formula above, we will need to express $\pm mP_n^m(x) + S_n^m(x)$ through $P_n^{m-2}(x)$ and $P_n^{m+2}(x)$ respectively, in order to be able to express $\mathcal{L}(\mathbf{I}_s)\Phi_{n,m}^i$ through basis functions $\Phi_{n,m}^i$. The following identities permit such operations (the first one is valid for all $m \geq 0$ and the second one for all $m \geq 2$):

$$\begin{aligned} -mP_n^m(x) + S_n^m(x) &= \frac{(n-2)}{(2n+1)(2n-1)}P_{n-2}^{m+2}(x) \\ &+ \frac{3}{(2n+3)(2n-1)}P_n^{m+2}(x) \\ &- \frac{(n+3)}{(2n+1)(2n+3)}P_{n+2}^{m+2}(x) \end{aligned} \quad (\text{A.4})$$

and

$$\begin{aligned} mP_n^m(x) + S_n^m(x) &= \frac{(n-2)(n+m)(n+m-1)(n+m-2)(n+m-3)}{(2n+1)(2n-1)}P_{n-2}^{m-2}(x) \\ &+ \frac{3(n+m)(n+m-1)(n-m+1)(n-m+2)}{(2n+3)(2n-1)}P_n^{m-2}(x) \\ &- \frac{(n+3)(n-m+1)(n-m+2)(n-m+3)(n-m+4)}{(2n+1)(2n+3)}P_{n+2}^{m-2}(x). \end{aligned} \quad (\text{A.5})$$

Replacing $\pm mP_n^m(x) + S_n^m(x)$ by their expression given by (A.4)-(A.5) in (A.3) we obtain the formulas (31).

A.2 Discretization of the operator $\mathbf{I}_s : \mathbf{uu}$

We now turn our attention to the operator $\mathbf{I}_s : \mathbf{uu}$. We note that

$$\mathbf{I}_s : \mathbf{uu} = \sin^2 \theta \cos 2\varphi$$

Denoting $x = \cos \theta$, we have thus

$$\begin{aligned} \mathbf{I}_s : \mathbf{uu}\Phi_{n,m}^i &= \frac{1}{2} \left[\cos \left((m+2)\varphi - i\frac{\pi}{2} \right) (1-x^2)P_n^m(x) \right. \\ &\quad \left. + \cos \left((m-2)\varphi - i\frac{\pi}{2} \right) (1-x^2)P_n^m(x) \right]. \end{aligned} \quad (\text{A.6})$$

As for the operator $\mathcal{L}(\mathbf{I}_s)$, we note the identities (the first one is valid for all $m \geq 0$ and the second one for all $m \geq 2$)

$$\begin{aligned}
(1-x^2)P_n^m(x) &= \frac{1}{(2n-1)(2n+1)}P_{n-2}^{m+2}(x) \\
&\quad - \frac{2}{(2n-1)(2n+3)}P_n^{m+2}(x) \\
&\quad + \frac{1}{(2n+1)(2n+3)}P_{n+2}^{m+2}(x)
\end{aligned}$$

and

$$\begin{aligned}
(1-x^2)P_n^m(x) &= \frac{(n+m-3)(n+m-2)(n+m-1)(n+m)}{(2n-1)(2n+1)}P_{n-2}^{m-2}(x) \\
&\quad + 2\frac{(n-m+2)(n+m-1)[m(m-1)-n(n+1)]}{(2n-1)(2n+3)}P_n^{m-2}(x) \\
&\quad + \frac{(n-m+1)(n-m+2)(n-m+3)(n-m+4)}{(2n+1)(2n+3)}P_{n+2}^{m-2}(x),
\end{aligned}$$

plug them into (A.6) and obtain (32).

References

- [1] R. C. Armstrong, R. Nayak and R. A. Brown, The use of kinetic theory and microstructural models in the analysis of complex flows of viscoelastic liquids, *Proceedings of the 12th International Congress on Rheology*, Laval university, Québec, Aug. 18-23, 1996, edited by Aït-Kadi, J.M. Dealy, D.F. James and M.C. Williams.
- [2] R. B. Bird, C. F. Curtiss, R. C. Armstrong, O. Hassager *Dynamics of polymeric liquids, vol. 2, Kinetic theory*, (2nd ed. Wiley-Interscience, New York, Chichester, Brisbane, Toronto, Singapore, 1987).
- [3] J. Bonvin, Numerical Simulation of Viscoelastic Fluids With Mesoscopic Models, *Ph.D. thesis*, École Polytechnique Fédérale de Lausanne, Lausanne, Switzerland, 2000.
- [4] J. Bonvin and M. Picasso, Variance reduction methods for CONNFFESSIT-like simulations, *J. Non-Newtonian Fluid Mech.* **84** (1999) 191-215.
- [5] C. Chauviere and A. Lozinski, Simulation of dilute polymer solutions using a Fokker-Planck equation, *Computers and Fluids*, to appear.
- [6] C. Chauvière and R. G. Owens, A new spectral element method for the reliable computation of viscoelastic flow, *Comput. Methods Appl. Mech. Engrg.* **90** (2001) 3999–4018.
- [7] H. S. Dou and N. Phan-Thien, The flow of an Oldroyd-B fluid past a cylinder in a channel: adaptive viscosity vorticity (DAVSS- ω) formulation, *J. Non-Newtonian Fluid Mech.* **87** (1999) 47-73.

- [8] Y. R. Fan and R. I. Tanner and N. Phan-Thien, Galerkin/least-squares finite-element methods for steady viscoelastic flows, *J. Non-Newtonian Fluid Mech.* **84** (1999) 233-256.
- [9] X. J. Fan, Viscosity, first normal-stress coefficient, and molecular stretching in dilute polymer solutions, *J. Non-Newtonian Fluid Mech.* **17** (1985) 125-144.
- [10] X. J. Fan, Viscosity, first normal-stress coefficients, and molecular stretching in concentrated solutions and melts, *J. Non-Newtonian Fluid Mech.* **17** (1985) 251-265.
- [11] X. J. Fan, Molecular models and flow calculation: I. The numerical solutions to multibead-rod models in inhomogeneous flows, *Acta Mech. Sin.* **5** (1989) 49-59.
- [12] X. J. Fan, Molecular models and flow calculations: II. Simulation of steady planar flow, *Acta Mech. Sin.* **5** (1989) 216-226.
- [13] M. A. Hulsen, A. P. G. van Heel, B. H. A. A. van den Brule, Simulation of viscoelastic flows using Brownian configuration fields, *J. Non-Newtonian Fluid Mech.* **70** (1997) 79-101.
- [14] A. Lozinski and C. Chauvière, A fast solver for Fokker-Planck equation applied to viscoelastic flows calculations: 2D FENE model, *J. Comput. Phys.*, 189(2) (2003) 607-625.
- [15] A. Lozinski, C. Chauvière, J. Fang, and R. G. Owens, A Fokker-Planck simulation of fast flows of concentrated polymer solutions in complex geometries, *J. Rheol.* **47** (2003) 535-561.
- [16] R. Nayak, Molecular simulation of liquid crystal polymer flow: a wavelet-finite element analysis, PhD thesis, MIT, Cambridge, MA. 374pp. (1998).
- [17] H. C. Öttinger, *Stochastic processes in polymeric fluids* (Berlin, Springer Verlag, 1996).
- [18] R. G. Owens and T. N. Phillips, Steady viscoelastic flow past a sphere using spectral elements, *Int. J. Numer. Methods Eng.* **39** (1996) 1517-1534.
- [19] N. Phan-Thien and H. -S. Dou, Viscoelastic flow past a cylinder: drag coefficient, *Comput. Methods Appl. Mech. Engrg.* **180** (1999) 243-266.
- [20] J. Sun, M. D. Smith, R. C. Armstrong and R. A. Brown, Finite element method for viscoelastic flows based on the discrete adaptive viscoelastic stress splitting and the discontinuous Galerkin method: DAVSS-G/DG, *J. Non-Newtonian Fluid Mech.* **86** (1999) 281-307.